Acta Oceanol. Sin., 2022, Vol. 41, No. 7, P. 113–127
https://doi.org/10.1007/s13131-022-1990-8
http://www.aosocean.com
E-mail: ocean2@hyxb.org.cn

Characteristics of sea ice kinematics from the marginal ice zone to the packed ice zone observed by buoys deployed during the 9th Chinese Arctic Expedition

Xiaomin Chang[1]*, Longchun Ye[1], Guangyu Zuo[2], Jingyue Li[1], Keyu Wei[1], Yinke Dou[2]

[1] College of Water Resources Science and Engineering, Taiyuan University of Technology, Taiyuan 030024, China

[2] College of Electrical and Power Engineering, Taiyuan University of Technology, Taiyuan 030024, China

Received 17 September 2021; accepted 9 November 2021

Abstract

Sea ice growth and consolidation play a significant role in heat and momentum exchange between the atmosphere and the ocean. However, few *in situ* observations of sea ice kinematics have been reported owing to difficulties of deployment of buoys in the marginal ice zone (MIZ). To investigate the characteristics of sea ice kinematics from MIZ to packed ice zone (PIZ), eight drifting buoys designed by Taiyuan University of Technology were deployed in the open water at the ice edge of the Canadian Basin. Sea ice near the buoy constantly increased as the buoy drifted, and the kinematics of the buoy changed as the buoy was frozen into the ice. This process can be determined using sea ice concentration, sea skin temperature, and drift speed of buoy together. Sea ice concentration data showed that buoys entered the PIZ in mid-October as the ice grew and consolidated around the buoys, with high amplitude, high frequency buoy motions almost ceasing. Our results confirmed that good correlation coefficient in monthly scale between buoy drift and the wind only happened in the ice zone. The correlation coefficient between buoys and wind was below 0.3 while the buoys were in open water. As buoys entered the ice zone, the buoy speed was normally distributed at wind speeds above 6 m/s. The buoy drifted mainly to the right of the wind within 45° at wind speeds above 8 m/s. During further consolidation of the ice in MIZ, the direct forcing on the ice through winds will be lessened. The correlation coefficient value increased to 0.9 in November, and gradually decreased to 0.7 in April.

Key words: sea ice, kinematics, buoy observations, remote sensing, marginal ice zone

Citation: Chang Xiaomin, Ye Longchun, Zuo Guangyu, Li Jingyue, Wei Keyu, Dou Yinke. 2022. Characteristics of sea ice kinematics from the marginal ice zone to the packed ice zone observed by buoys deployed during the 9th Chinese Arctic Expedition. Acta Oceanologica Sinica, 41(7): 113–127, doi: 10.1007/s13131-022-1990-8

1 Introduction

The marginal ice zone (MIZ), a buffer between open water and ice pack, spans from where 15% of the sea surface is covered by ice to 80% ice concentration (Aksenov et al., 2017; Strong and Rigor, 2013). MIZ plays a key role in marine ecosystems and its time-varying state affects the exchange of ocean-atmosphere (Liu et al., 2021; Vichi et al., 2019; Taylor et al., 2013). Abrupt climate changes have been observed in the Arctic over the last 40 years, the current Arctic sea ice is transitioning from a thick, strong ice pack to a thinner, more fragile ice cover (Stroeve et al., 2012; Rampal et al., 2009). Furthermore, ice-free summers have a high probability in the Arctic by the middle to the end of the 21 century in response to the increasing greenhouse gas concentrations (Notz and Community, 2020). The measurements of sea ice growth and drift are crucial for understanding the ocean–ice–atmosphere system in the MIZ. The formation of sea ice reduces upper ocean stability and modifies the atmospheric boundary layer. Consolidation of sea ice causes ridges and leads, affecting the local sea ice thickness (Itkin et al., 2018). Leads between ice floes increase heat loss from the ocean to the atmosphere (Alam and Curry, 1998). This process is extremely important in winter for promoting under-ice haptophyte algae blooms (Assmy et al., 2017) and is highly related to the Arctic amplification (Lüpkes et al., 2008). The rapid shrinking of sea ice cover in the Arctic results in the MIZ expanding (Boutin et al., 2020; Lee et al., 2017; Strong et al., 2017), and this may bring more challenges to the exploration of sea ice changes.

The formation of sea ice in the Arctic is strongly coupled with the ocean and atmosphere. Small frazil crystals begin to form when the ocean surface is at or slightly below the freezing point. The consolidation of sea ice crystals can form under two different modes, depending on the wind and wave conditions (Weeks and Ackley, 1986; Shen and Ackley, 1991). The process of how new ice forms is not well understood, as the nature size of the ice makes its study difficult. Satellite remote sensing has long been used to derive sea ice drift speed from pairs of sequential images. However, it can hardly be used in the detection of sea ice growth, mainly because of the small size of new ice. Sea ice models, such as CICE5 and LIM3, usually employ a probability distribution in sea ice thickness to calculate thermodynamic and dynamic sea ice evolution. This may result in uncertainty estimates in a complex area, such as the MIZ. Buoys are typically used to character-

Foundation item: The National Key Research and Development Program of China under contract No. 2016YFC1402702; the Basic Research Program of Shanxi Province under contract No. 202103021224054.
*Corresponding author, E-mail: changxiaomin@tyut.edu.cn

ize the changes in sea ice thermodynamics and the spatial and temporal variations of ice deformation (Zuo et al., 2018a, 2018b; Yu et al., 2021). To accurately describe the ice motion occurs in small scales and over short periods, the *in situ* data like collected by the buoys is still needed (Hutching and Hibler, 2008). However, the inaccessibility of polar regions and harsh wave-influenced environments leads to fewer studies on sea ice growth processes than for melt processes.

To analyze the dynamic difference between the new ice and the pack ice, an array of drifting buoys was deployed in a "five dice" pattern by Doble and Wadhams (2006). Compared to the wave height and mean period between the buoys outer and inner ice edges, whether the ice near buoys consolidated can be judged. This method gives the exact time of sea ice consolidation, but the field arrangement of the experiment is demanding and complicated. To reduce the deployment of buoys in the packed ice zone (PIZ), Roach et al. (2018b) quantified the ice growth by using images from drifting buoys. Lund et al. (2018) presented new ice drift fields measured by shipboard radar. These methods simplified the experiment, and the results are more reliable. The former focuses on the changes in sea ice status and has a shorter study period of about a week. And the latter ice speed calculated by radar images and reference sea ice drift remains error. Coupled to the ice thickness distribution (ITD) theory, Zhang et al. (2015) developed an floe size distribution (FSD) theory to explicitly simulate the evolution of FSD and ITD jointly. Horvat and Tziperman (2017) discussed sea ice floe size distribution through numerical experiments. This could explain the distribution and evolution of sea ice, but explanations for changes in sea ice movement are still lacking.

The aim of the present works is mainly to focus on the process from the new ice to the packed ice, the characteristics of newly formed packed ice kinematics have thus remained largely unknown. In this study, observations from buoys deployed in the Canadian Basin during the 9th Chinese National Arctic Research Expedition (CHINARE) in 2018 are reported. This paper was designed to provide a method for the new ice evolved from unconsolidated ice to the packed ice. The buoys data was used to investigate the characteristics of the sea ice kinematics between the MIZ and PIZ, which includes the dynamics of packed ice after consolidation. The time when buoys enter the packed ice is discussed in Section 3. In Section 4, the spatiotemporal changes in the atmosphere and its impact on the wind heading distribution are described. Section 5 analyses the speed changes of buoys, investigates the drift of buoys in response to the wind in different ice conditions, and calculates the inertial oscillation. The discussion and conclusions are presented in Section 6 and Section 7, respectively.

2 Data and methods

2.1 *Deployment of drifting buoys*

The location data used in this study was transmitted by Taiyuan University of Technology (TUT) buoys, which are drifting buoys equipped with GPS. TUT buoy is composed of a surface float, a tether, and a drogue (Fig. 1a). The length and the diameter of the drogue are 10 m and 0.6 m, respectively. The diameter of the drogue hole is 0.3 m, and the depth interval is 1.6 m, which can be used to capture the flow rate and direction of the ocean current (Manda et al., 2002). Moreover, an annular steel ring is installed at the bottom to support the structure and counterweight of the drogue. The length of corrosion-resistant tether assembly is 5 m, and is used to connect the drogue to the float. TUT buoy remained in the ice as ice consolidated into a coherent ice sheet. The surface floating with a sphericity shape can rectify the surface wave as the net horizontal force, and significantly reduce the damage of sea ice freezing to the buoy. The diameter of the floating ball located on the water surface is 0.4 m, which is equipped with an Iridium satellite module, a global navigation and positioning module, an antenna and a battery unit. The data was sent to the satellite network via the Iridium network and stored in an SBD format with sampling intervals of 1 h. Prior to deployment, the horizontal position accuracy for all TUT buoys was calibrated on the ice breaker *Xuelong*. The standardization took place over a week with the maximum deviation of horizontal position among the GPS being below 5 m. During the 9th CHINARE, eight TUT buoys were deployed around late July 2018 between 154°W and 165°W along 75°N (Fig. 1b).

The study region was defined as 70°–85°N, 170°E–140°W (Fig. 2a). All buoys were deployed in open water upon deployment, as confirmed by observers onboard the ice breaker *Xuelong*. After deployment, the buoys moved westward and then towards the

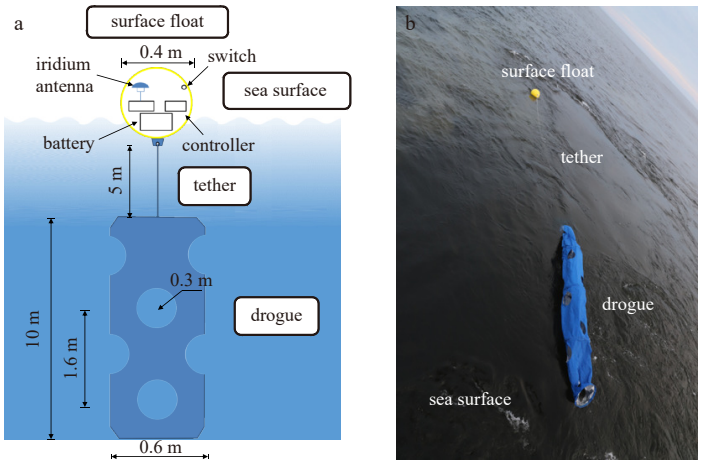

Fig. 1. Taiyuan University of Technology (TUT) buoy mainly consists of surface float, a tether and drogue. The surface float is responsible for sending position data, drogue pulls the float by the tether with the ocean current as buoy in the open water. a. Schematic depiction of TUT buoy; b. Buoy A, shortly after deployment at the site of 74.63°N, 164.95°W with the drogue floated on the sea.

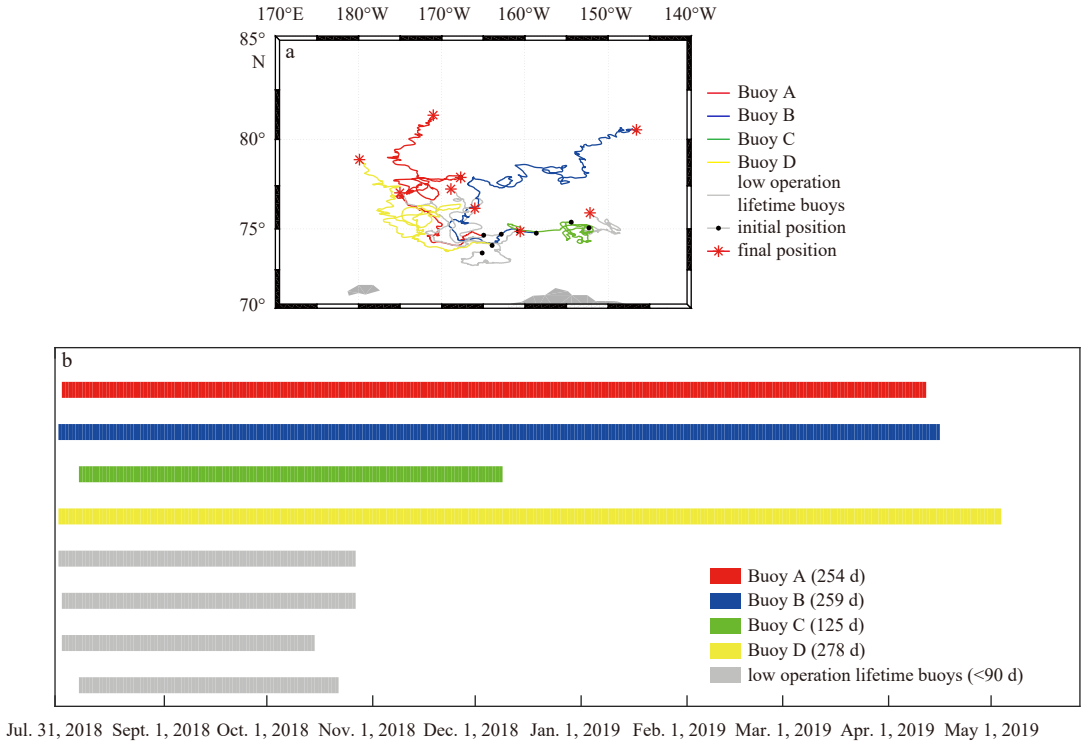

Fig. 2. Operation of the buoys deployed in the 9th Chinese National Arctic Research Expedition (CHINARE). a. Map of all eight Taiyuan University of Technology (TUT) buoys drift tracks in 2018–2019; deployment locations (black point) and final position (red asterisk) are shown; b. time series of observations by all eight TUT buoys deployed during the 9th CHINARE.

north of the Canada Basin under ocean currents and wind force. Operation periods of all TUT buoys are shown in Fig. 2b. The first buoy stopped working on October 2, 2018. The operation time of four buoys (grey) was below three months owing to battery problems caused by the terrible weather, unfortunately. The other four buoys recorded the motion changes in the process of sea ice growth and consolidation successfully, which were named Buoys A, B, C, and D. Three buoy operation lifetimes were even close to nine months. Ultimately, five buoys survived during the ice season; of these buoys, only four buoys entered the ice zone. The last buoy (Buoy D) stopped working on May 2, 2019. Most subsequent discussions of buoys include only these four. The drift trajectories in the Canadian Basin do not follow smooth straight lines, but instead describe curves and loops. This results from the variability of atmospheric forcing are due to the passage of synoptic weather systems (Haller et al., 2014; Heil et al., 2008).

2.2 *Buoy kinematic characteristics*

The buoy sampling interval is 1 h; and the accuracy δ_v of the buoy velocity (Leppäranta, 2011) is

$$\delta_v = \sqrt{2s^2/\Delta t^2}, \tag{1}$$

where s is the horizontal position accuracy and Δt is the interpolation interval. The accuracies of the daily and hourly buoy velocities are therefore 0.03 cm/s and 0.6 cm/s, respectively.

To determine the status of buoy movement, the 3.125 km× 3.125 km gridded sea ice concentration data provided by the University of Bremen (www.seaice.uni-bremen.de) was used. The data was derived from the brightness temperature field obtained from the Advanced Microwave Scanning Radiometer-2 (Spreen et al., 2008). For other atmospheric variables such as wind velocity at a height of 10 m ($W_{10\ \mathrm{m}}$), sea level pressure (SLP), and skin temperature (SKT), the ERA5 reanalysis data with a 0.25°×0.25° resolution provided by the European Centre for Medium–range Weather Forecasts were used (Delhasse et al., 2020; Clem et al., 2020). Sea ice concentration data were bilinearly interpolated to the daily position of the buoy, and the other data sets were bilinearly interpolated to the hourly position of the buoys (Lei et al., 2016).

Despite the underlying principle between the ice concentration and the mechanical behavior of the cover, it still needs to be quantified. Promoted by the observation of the Fram's journey along the transpolar drift. Nansen (1902) made the first studies of oceanic inertial oscillations. It was found that sea ice moved with a 20°–40° angle to the right of the wind heading. According to Gimbert et al. (2012b), the coriolis force acts perpendicularly to particle velocity resulting in the deviation of trajectories to the right in the Northern Hemisphere.

The normalized amplitude at the inertial frequency (Lei et al., 2016) was used to characterize the frequency-domain signal of the buoy velocity. The value can indicate the free–drift property of the buoy motion. To obtain this value, we applied Fourier analysis using a fast Fourier transformation algorithm for normalized hourly velocities for Buoys A, B, C, and D. Along the buoy trajectories, the absolute magnitude of buoy velocity may change. Normalized velocities were provided to better compare the frequency-domain signals. To reduce the influence of long time scale, low-frequency signals, a three-day sliding temporal window was applied to calculate the normalized velocities. The frequency of the inertial oscillation depends on the particle latitude,

$$f_0 = 2\Omega \sin\phi, \tag{2}$$

where f_0 is inertial frequency, Ω is the Earth rotation rate, and ϕ is latitude. The inertial frequency ranges from 1.88 cycles/d to 2.00 cycles/d between 70°N and 85°N, which is, close to a semi-diurnal frequency (2 cycles/d).

Fourier analysis was used to calculate rotary spectra from buoy velocity to identify signals of inertial and tidal origin, both of which have a frequency of 2 cycles/d in the Arctic Ocean. The complex Fourier transformation $\widehat{U}(\omega)$ is defined as follows:

$$\widehat{U}(\omega) = \frac{1}{N}\sum_{t=t_0}^{t_{\mathrm{end}}-\Delta t} \mathrm{e}^{-\mathrm{i}\omega t}(U+\mathrm{i}V), \tag{3}$$

where N is the number of velocity samples, t_0 and t_{end} are the start and end times of the temporal window; U and V are the zonal and meridional speeds at t+0.5Δt on an orthogonal geographical grid; and ω is the angular frequency.

The meander coefficient (MC) was applied to evaluate the effective translation associated with the buoy drift. An MC of one means that the buoy trajectory is a straight line, with high values resulting in highly unstable trajectory. Here, we calculate the monthly MC, which is the ratio of the accumulation of hourly buoy displacement to the net displacement.

3 Determination of ice consolidation

The primary aim of the analysis is to contrast the dynamics of buoys in the open ocean with those of consolidated pack ice. We therefore need to determine when the seawater around the buoy starts to freeze. The variation of sea ice growth at the buoy location can be reflected by sea ice concentration. On August 1, 2018, distribution of sea ice in the study area showed spatial heterogeneities, the concentration of sea ice in the western part of the study area was much higher than that in the east. Seawater froze, formed small frazil crystals and then consolidated to the pack ice during the frozen season. This process was captured and recorded in the form of position data by the TUT buoys. The ice concentration near the buoys showed a rapid increase in mid-October and remained high (Fig. 3). The exact date of consolidation for each buoy was inferred from changes of the ice concentration and the skin temperature. This was caused by the growth of sea ice, which altered the drift characteristics of buoys (discussed in Section 5). At this juncture, four of the eight buoys (low operation lifetime buoys) failed to withstand the strong environmental conditions and stopped working, and the spatial difference in sea ice concentration gradually decreased.

The SKT and sea ice concentration near the four buoys underwent similar changes due to their close deployment positions. From August to October 2018, the SKT near the buoys was maintained at about –1°C. From mid-October 2018 onwards, the daily average SKT dropped sharply and remained below –1.8°C throughout the buoy life. This is consistent with variation of the sea ice concentration, demonstrates the thermodynamic ice growth. At the Buoy D site, the SKT increased markedly after mid-April. This is mainly due to the sea ice melting and breaking up.

4 Spatiotemporal changes in atmospheric conditions

In winter, the Arctic atmosphere is influenced by two major circulation systems (Timmermans and Marshall, 2020). The Beaufort Gyre (BG) is one of the two major ocean currents in the Arctic Ocean. It is roughly located north of the Alaskan and Canadian coasts. In the past, Arctic sea ice circulated in the BG for up to several years, leading to the formation of very thick multi-year sea ice. Because of the Arctic amplification, the gyre has lost a considerable amount of ice, with the oldest, thickest ice gradually disappearing (Howell et al., 2008).

The circulation in the western Arctic is characterized by a quasi-stationary region of high pressure known as the Beaufort High (BH). Although it is usually connected to the Siberian High through a ridge of high pressure, the BH is normally a closed anticyclone during winter (Serreze and Barrett, 2011). To identify the influence of atmospheric circulation patterns on sea ice kinematics, the Arctic oscillation (AO) and BH indices were calculated to relate the strength of the BG. In addition, the central Arctic index (CAI) and dipole anomaly (DA) index were calculated to relate the potential of the northward advection of sea ice from the study region to the Atlantic sector of the Arctic Ocean (Lei et al., 2021).

Monthly SLP data north of 70°N obtained from the NCEP/NCAR reanalysis I was used to calculate the empirical or-

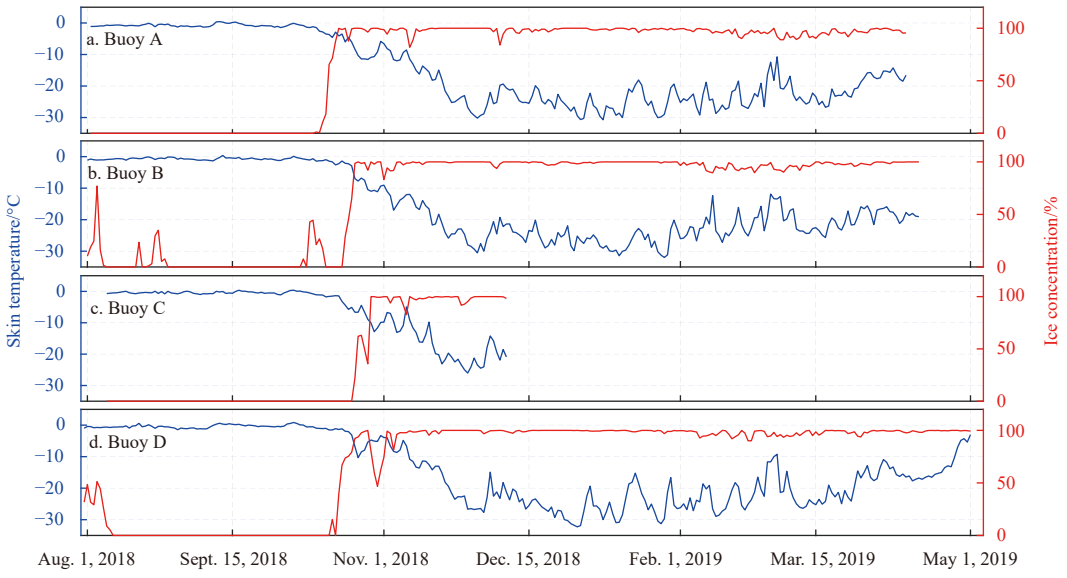

Fig. 3. Ice concentration (red) and skin temperature (blue) near Buoys A–D during the operation period.

thogonal function modes, with the AO index and DA index as the first and second modes (Wang et al., 2009). The CAI was defined as the difference in SLP between 90°W and 90°E at 84°N (Vihma et al., 2012). The BH index was calculated as the average SLP anomaly over the domain of 75°–85°N and 170°E–150°W (Moore et al., 2018) relative to 1979–2018 climatology.

The CAIs for August, September and October 2018 were moderate. In the following six months, the magnitude of the CAI was notably positive and even reached 11.6 hPa in February, ranking second highest in 1979–2019. The AO index was strongly positive in August 2018, February and March 2019, and in November 2018, it was much lower at –1.1, ranking seventh in 1979–2018 (Fig. 4). The BH index for December 2018, February and March 2019 was strongly negative, ranking sixth, second and fourth lowest in 1979–2019, respectively. The DA index was low in August 2018 and remained positive over the next eight months. In November 2018 and January 2019, the DA index was positively high, ranking sixth highest in 1979–2018. In February 2019, the rank changed to the third lowest in March 2019, with a value of 1.1 (Fig. 5).

Regarding the change in the BH index and AO index, there was a distinct contrast in the BG pattern between months with significant changes. With a positive high value, the wind vectors were generally clockwise in August and September 2018. In contrast, the wind vectors changed to counterclockwise when the value was high and negative, for example, in February 2019. When the value alternately switched from positive to negative in adjacent months, wind vectors in the north of the study area were clockwise and anticlockwise in the south. Associated with the change in CAI and DA index, the distribution of strong northerly winds had a significant contrast between different months. In August 2018, nearly no northerly winds appeared in the study area, with a CAI value of –5.0. In the months with a strongly positive CAI and DA index, enhanced northerly winds prevailed across most of the study area (Fig. 5).

As seen in Fig. 6, the $T_{2\,\mathrm{m}}$ average anomalies show a signific-

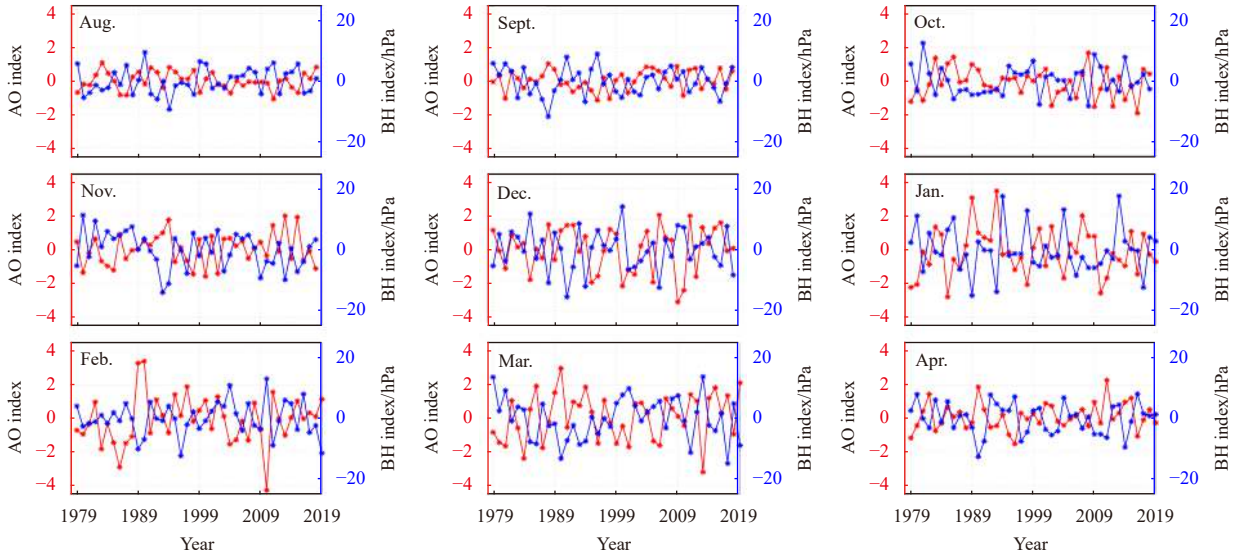

Fig. 4. Changes in monthly Arctic oscillation (AO) index (red) and monthly Beaufort High (BH) index (blue) from August to April in 1979 –2019.

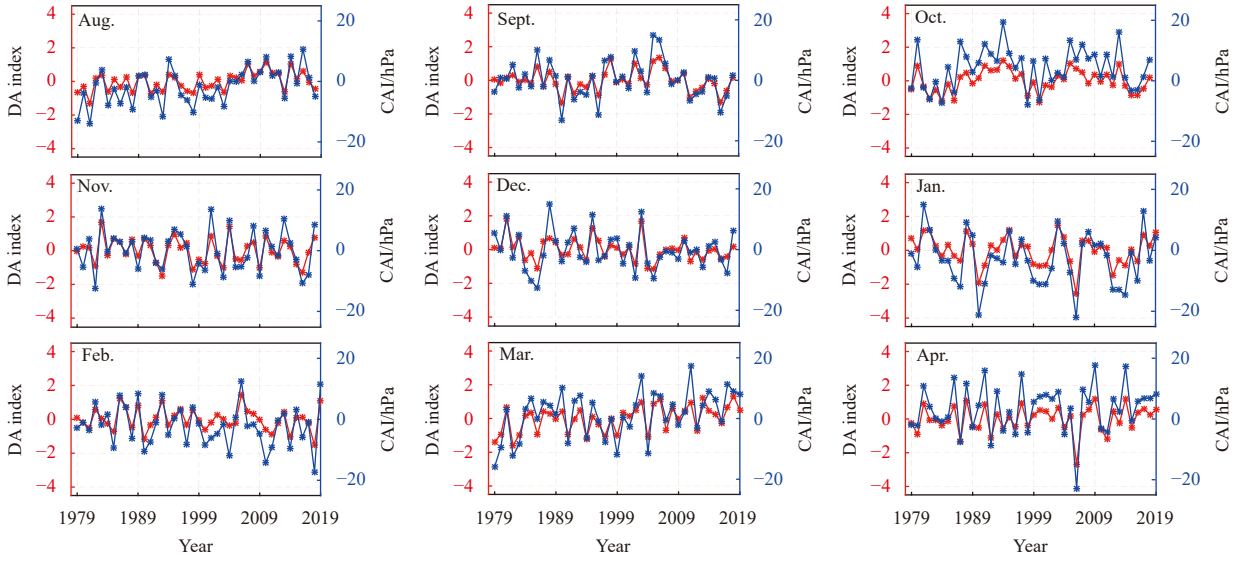

Fig. 5. Changes in monthly dipole anomaly (DA) index (red) and monthly central Arctic index (CAI) (blue) from August to April in 1979–2019.

ant difference between autumn and winter in 2018 over the study area. The average $T_{2\,m}$ anomalies in autumn 2018 (3.0°C, 6.7°C, and 2.7°C for September, October, and November, respectively) were strongly positive, while they were much lower for the following winter (0.1°C, −0.6°C, and 3.3°C for December, January, and February, respectively). This can be ascribed to the seasonality of the Arctic amplification (Screen et al., 2018). With the largest sea ice reduction that occurred in summer and early fall, ice growing rapidly resulted in the strongest surface warming in October 2018. In Fig. 6, the buoy trajectories are not consistent with the wind direction in the first few months, and mainly depend on the ice concentration. After October 2018, the buoy drift and wind direction were significantly higher.

5 Results

5.1 *Buoy velocity*

All TUT buoys were initially deployed in the open water, the position data transmitted by the surface float reflects the speed of the ocean current. TUT buoys remained in and moved with the sea ice as seawater around the buoys frozen and consolidated. This process is recorded by the speed information of the TUT buoy. The drifting speed of four buoys was calculated and plotted in Fig. 7. A dramatic contrast was seen when buoys entered the ice zone (mid-October). The high amplitude and high frequency buoy motions ceasing rapidly and reappearing as sea ice concentration decreases due to few episodic warm events. Compared to the open water, the drift speed values were lower where buoys were in the ice zone. The monthly drift speed values were approximately 0.15 m/s, when buoys were in the open ocean between August and September. The values showed a decreasing trend from October to February with buoys in the middle Canadian Basin. During this period, the buoys underwent a transition from ocean drift to ice drift in which sea ice growth slowed the buoy drift. Drift speed suddenly increased in February 2019, possibly because of broken ice and sea ice lead (Willmes and Heinemann, 2016; Qu et al., 2021; Beitsch et al., 2014; Lei et al., 2020). This also reflects the changes in the SKT and sea ice concentration. Subsequently, the speed dropped to around 0.05 m/s and 0.03 m/s in March and April, respectively, which is comparable with the average ice velocity for the entire Arctic Ocean (Haller et al., 2014). The drift speed decreased by a factor of five from the open ocean to the ice zone. It is difficult to distinguish regional and seasonal differences from buoy observations; however, the result by a factor of five is much more remarkable than the typical seasonal ice drift speed variation.

The changes in the wind direction led to irregular changes in the buoy drift direction, which results from the variability of atmospheric forcing due to the passage of synoptic weather systems. Applying longer resampling intervals to buoy position data may filter out ice motion at higher frequencies (Zhang et al., 2012), resulting in reduced buoy speed (Fig. 8). For example, the drift speed of Buoy A in August 2018 was 0.18 m/s at a resampling interval of 1 h, and decreased to 0.14 m/s at a resampling interval of 72 h. The other buoy data also showed similar variations. A more consolidated ice pack and relatively weak wind forcing as a result of a dominant high-pressure system led to buoy drift speed reaching minimums for the winter from December 2018 to Janu-

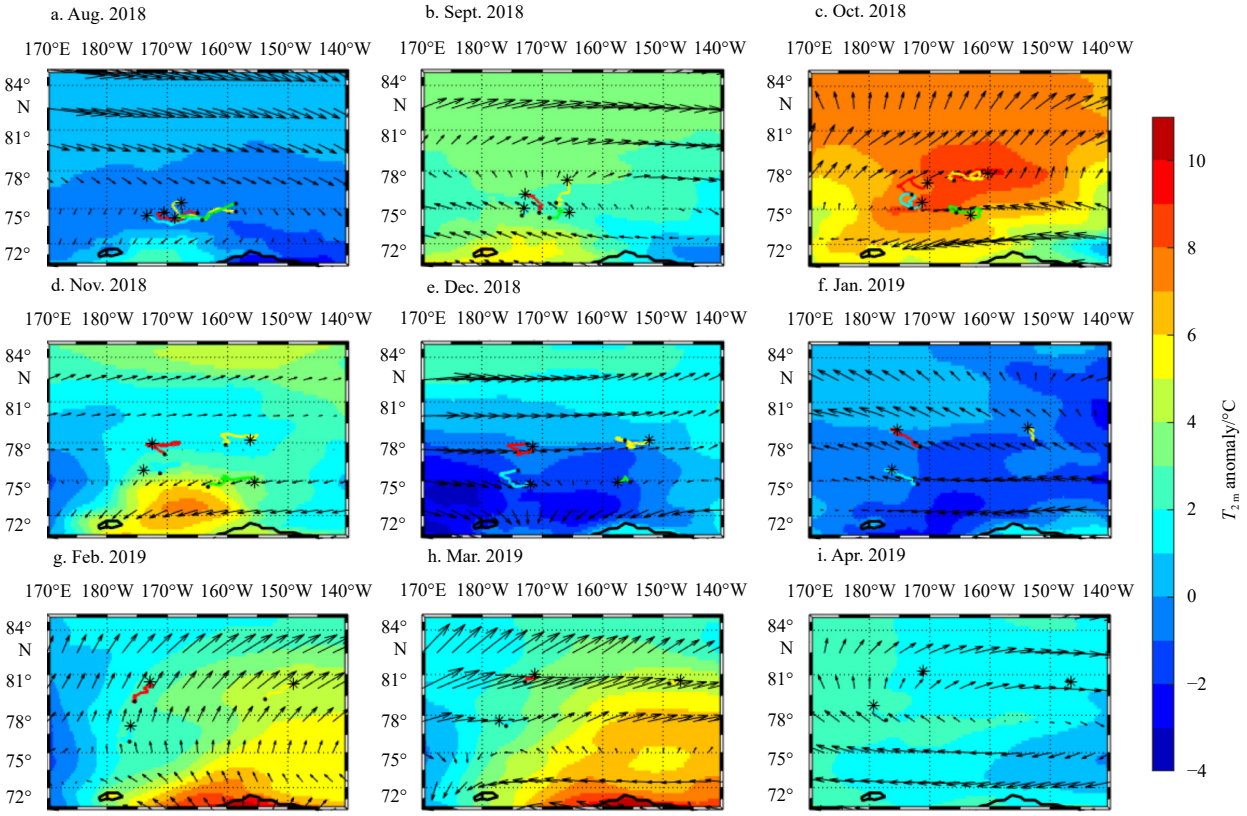

Fig. 6. Anomalies of near-surface air temperature ($T_{2\,m}$) over the Canadian Basin during August 2018 and April 2019 relative to 1979–2018 climatology; arrows indicate monthly average wind vectors (black) and trajectories of Buoy A (yellow), Buoy B (green), Buoy C (blue) and Buoy D (red). The points and asterisks represent the intial locations and final positions of the buoys in different months, respectively.

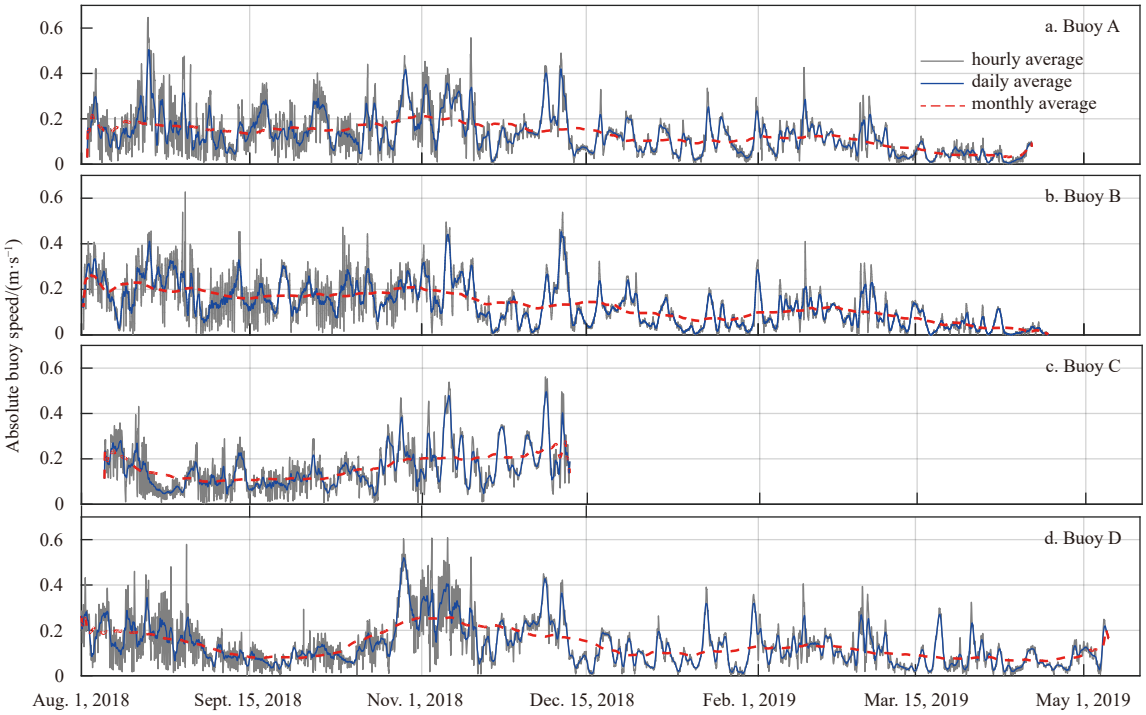

Fig. 7. Variations in buoys velocities measured by Buoys A–D are plotted with 1 h resolution (grey solid), 1 d resolution (blue solid) and with monthly filter (red dash). High amplitude and high frequency buoy motions ceasing rapidly after buoy entered the ice zone (mid-October).

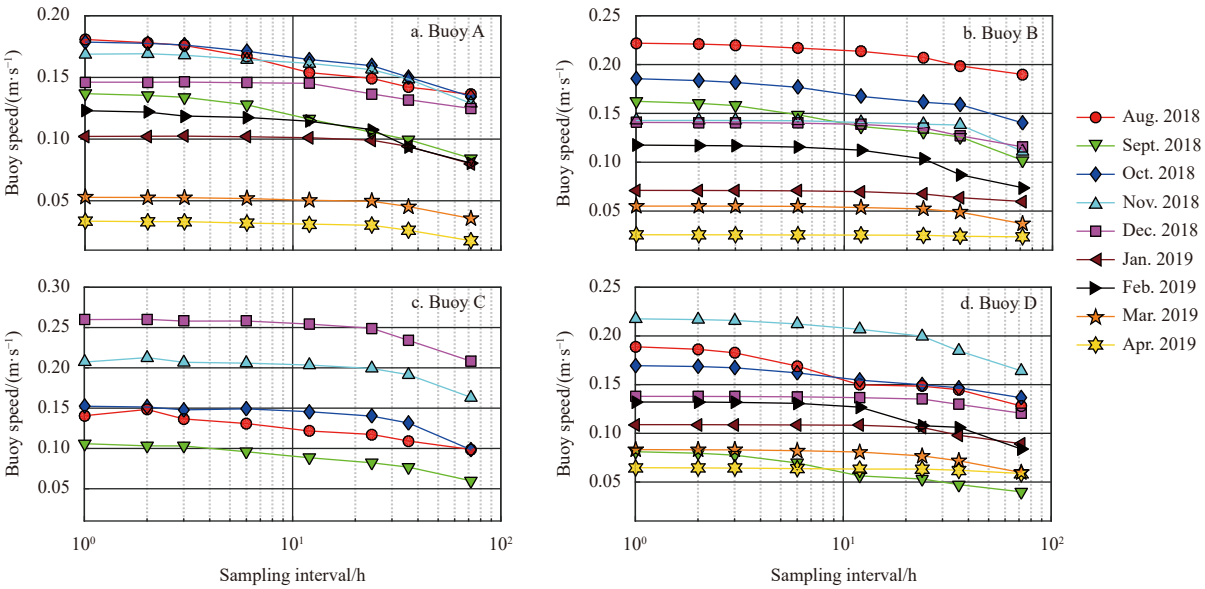

Fig. 8. Speed changes in Buoys A–D as a function of position data resampling interval for various months in 2018 and 2019.

ary 2019. The value continued to decrease in the two months after February 2019. Temporal resampling had little effect on the buoy speed during the freezing season. This means that meandering and sub-daily oscillations in the drift were substantially reduced in this period. Significantly, the resampling intervals have a large impact on the drift speed of buoys in February 2019.

5.2 *Responses to surface wind*

The correlation coefficient between buoy speed and wind speed was remarkably related to the buoy working environment. As noted by the ice concentration shown in Fig. 3, all the buoys were drifting in the open water between August and September 2018, and the correlation coefficient value between buoy speed and wind speed remained low (0.10–0.39) while the buoy speed was high (8.1–22.1 cm/s, shown in Fig. 9). In mid-October, all the buoys started drifting to the ice edge, and the value of the correlation coefficient rapidly increased in the following months (0.77–0.91) and reached a maxima for the entire study period in November or December 2019. The value remained above 0.62 until the end of the study period. This occurred for the consolidation of ice and relatively weak wind forcing as a result of the domination of a high-pressure system. The MC among buoys showed

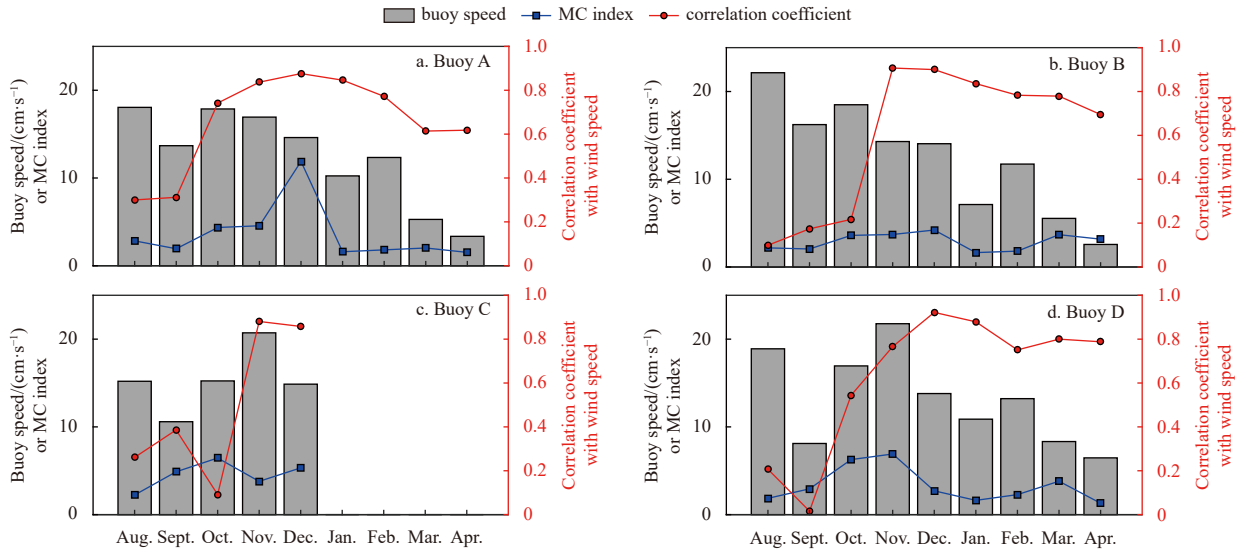

Fig. 9. Monthly average speed (left *y* axis, grey bar), monthly average meander coefficient (left *y* axis, blue line) and correlation coefficient between buoy speed and wind speed (right *y* axis, red line) among Buoys A–D. MC: meander coefficient.

that buoy trajectories were tortuous, especially from October to December 2018 (4.2–11.9).

Wind is the main driving force for ice drift over synoptic to climate timescales (Vinje, 2001; Uotila et al., 2000). The relationship between ice drift and wind is often represented in literature by the wind factor, WF (ratio buoy drift vs. wind). The absolute value of the turning angle between the drift vector and wind heading was used to classify the drift, following Vihma et al. (2012) Angles within 45° were assigned as "with wind heading", angles between 45° and 135° as "perpendicular to wind heading", and angles larger than 135° as "against wind heading". Here, the WF and absolute value of the turning angle were used to describe the relationship between buoy and wind, and the characteristics of buoy movement change.

The angle between the buoy drift direction and wind heading changed with time. Taking Buoy D as an example, it had the longest work time and the most complete data. Table 1 summarises the statistical relationship between buoy drift and surface wind speed based on hourly data. The buoy drift speed was 1.4%–3.1% of the surface wind speed between August and mid-October 2018, when the buoy drifted in the open ocean and had a low correlation coefficient with the wind speed. During this period, the angle between the buoy drift and wind vectors had no significant distribution characteristics. The ratio increased markedly in the next few months to 2.0%–3.2% and finally decreased to 1.4%–1.5% between March and April 2019. The increase was mainly related to the change in the working environment; buoys drifted from the open ocean to the ice and increased the correlation coefficient with the wind speed. The buoy drift with wind heading (79.4%–90.0%) exceeded that perpendicular to or against the wind vector. The ratio remained low between March and April because of lower wind speed and the majority of buoy drift (70.6%–75.1%) was decreased but still in the direction of the wind. Compared to Buoy D, the general trends of Buoys A–C were the same. However, the WFs of Buoys A–B (3.0–3.6) were higher than those of Buoys C–D (1.9–2.2) in

Table 1. Statistical relationships between buoy drift and surface wind vectors for Buoy D

	WF/%	Buoy drift with wind ($\alpha \leqslant 45°$)			Buoy drift perpendicular to wind ($45° < \alpha \leqslant 135°$)			Buoy drift in opposition to wind ($\alpha > 135°$)		
		P/%	$\overline{V}$/(m · s^{-1})	$\overline{V}_w$/(m · s^{-1})	P/%	$\overline{V}$/(m · s^{-1})	$\overline{V}_w$/(m · s^{-1})	P/%	$\overline{V}$/(m · s^{-1})	$\overline{V}_w$/(m · s^{-1})
Aug. 2018	3.6	41.0	0.193 (±0.104)	6.478 (±2.199)	48.6	0.191 (±0.087)	5.498 (±1.868)	10.4	0.160 (±0.073)	5.753 (±2.299)
Sept. 2018	1.9	32.5	0.077 (±0.035)	5.592 (±2.214)	50.3	0.085 (±0.044)	6.488 (±2.737)	17.2	0.075 (±0.041)	4.743 (±2.727)
Oct. 2018	3.1	46.6	0.245 (±0.137)	7.327 (±2.759)	38.0	0.108 (±0.055)	6.049 (±2.420)	15.4	0.092 (±0.039)	4.645 (±1.651)
Nov. 2018	3.4	83.8	0.233 (±0.106)	7.335 (±2.334)	15.4	0.143 (±0.095)	4.524 (±2.803)	0.8	0.075 (±0.016)	1.304 (±0.745)
Dec. 2018	2.3	87.1	0.150 (±0.106)	5.833 (±2.649)	12.8	0.058 (±0.043)	3.535 (±1.746)	0.1	0.030 (±0.005)	0.947 (±0.623)
Jan. 2019	1.9	79.3	0.127 (±0.083)	6.266 (±2.871)	18.0	0.041 (±0.031)	2.754 (±1.030)	2.7	0.024 (±0.015)	2.147 (±0.593)
Feb. 2019	2.2	90.0	0.134 (±0.066)	6.796 (±2.218)	9.5	0.117 (±0.075)	5.089 (±3.415)	0.5	0.065 (±0.027)	1.761 (±2.280)
Mar. 2019	1.4	75.1	0.089 (±0.065)	5.788 (±2.219)	23.7	0.070 (±0.069)	4.852 (±2.036)	1.2	0.014 (±0.006)	1.907 (±0.946)
Apr. 2019	1.6	70.6	0.078 (±0.037)	5.271 (±2.186)	26.6	0.033 (±0.014)	2.635 (±1.307)	2.8	0.023 (±0.012)	2.063 (±0.815)

Note: WF is the ratio between the buoy speed and wind speed; P is the probability of the turning angle between the buoy drift and the wind vectors; $\overline{V}$ is the mean buoy drift speed with SD in parentheses; $\overline{V}_w$ is the mean surface wind speed, with SD in parentheses.

September 2018. The WFs of Buoys A–B (0.7–1.2) were lower than that of Buoy D (1.4–1.6) between March and April 2019. This may be due to the different spatial distributions of wind and sea ice.

In addition to the wind speed, there was a special relationship between the wind heading and the direction of the buoy during the study period (Fig. 10). As illustrated by Buoy D, the distribution of buoy drift direction and the wind heading had a notable difference in the first three months during the buoy working period. The buoys did not follow the wind direction. However, this situation changed quickly. From November, the direction of buoy drift remained within a narrow range around 22.5° to the right of the wind, in agreement with a tight wind heading. This is consistent with the phenomenon of sea ice drift in response to wind from previous studies (Lei et al., 2016).

According to the results of Buoy D, the buoy movement changed, which can be attributed to multiple factors. The sea ice concentration surrounding the buoys increased from 0 to over 95% and took only a few days as shown in Fig. 3. To verify the influence of the working environment on the buoy drift, we divided the time data into two groups according to whether the ice concentration was greater than 50%. Statistics were used to study the buoy response to wind in different environments to reduce the impact of seasonal winds. The wind speed was divided into eight sections with a magnitude of 2 m/s. Drift-wind dir equals to buoy drift direction minus the wind vectors, is the turning angle (Lund et al., 2018).

Figures 11 and 12 show the buoy drift speeds at different wind speed magnitudes. In Fig. 11, the buoy drift speed is mainly distributed from 0.1–0.3 m/s with sea ice concentration below 50%. The ratio of the buoy drift speed and wind speed reached a stag-

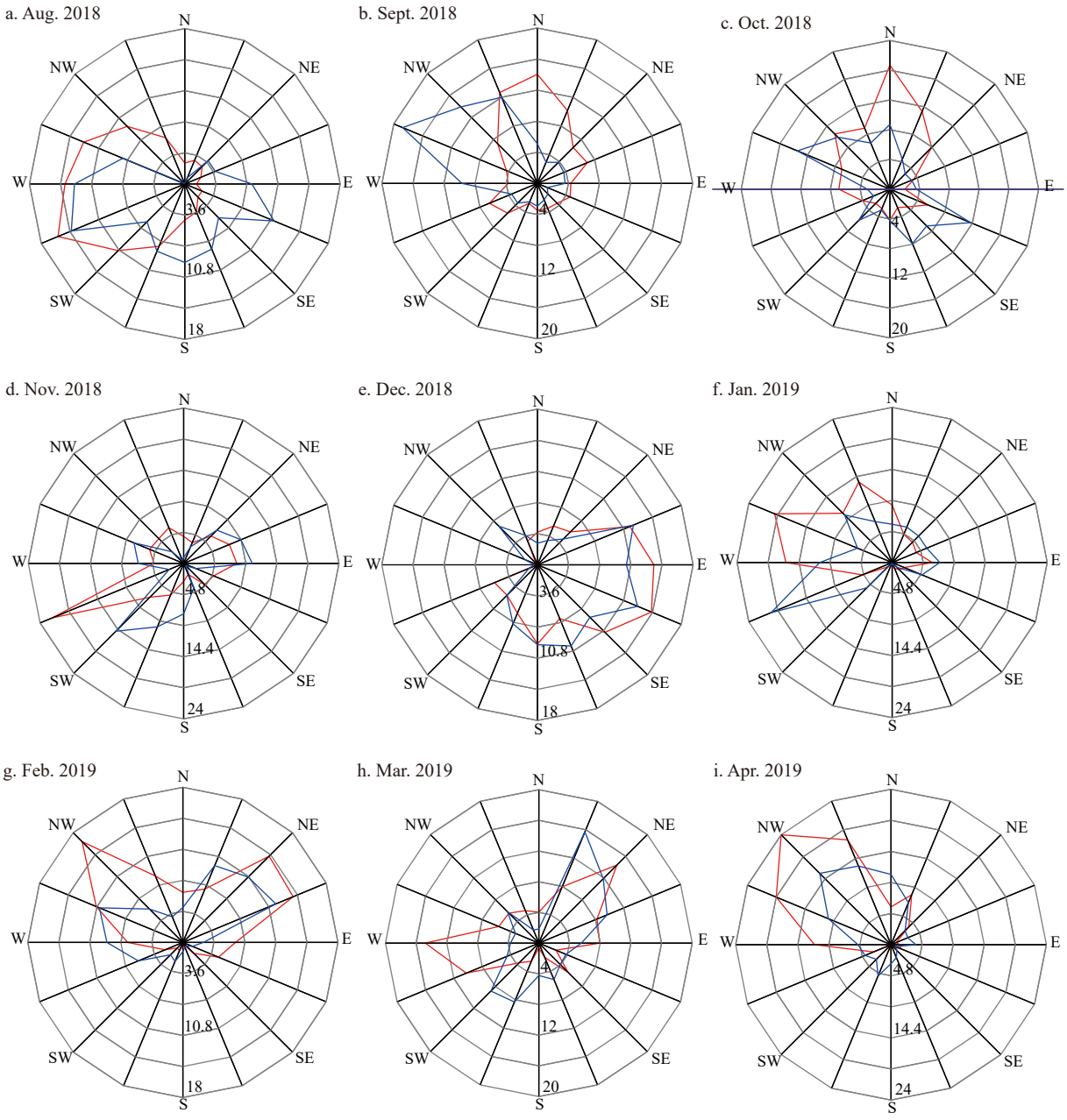

Fig. 10. Monthly direction distributions (%, scaled by numbers in black) of wind heading (blue) and buoy drift (red) at Buoy D from August 2018 to April 2019.

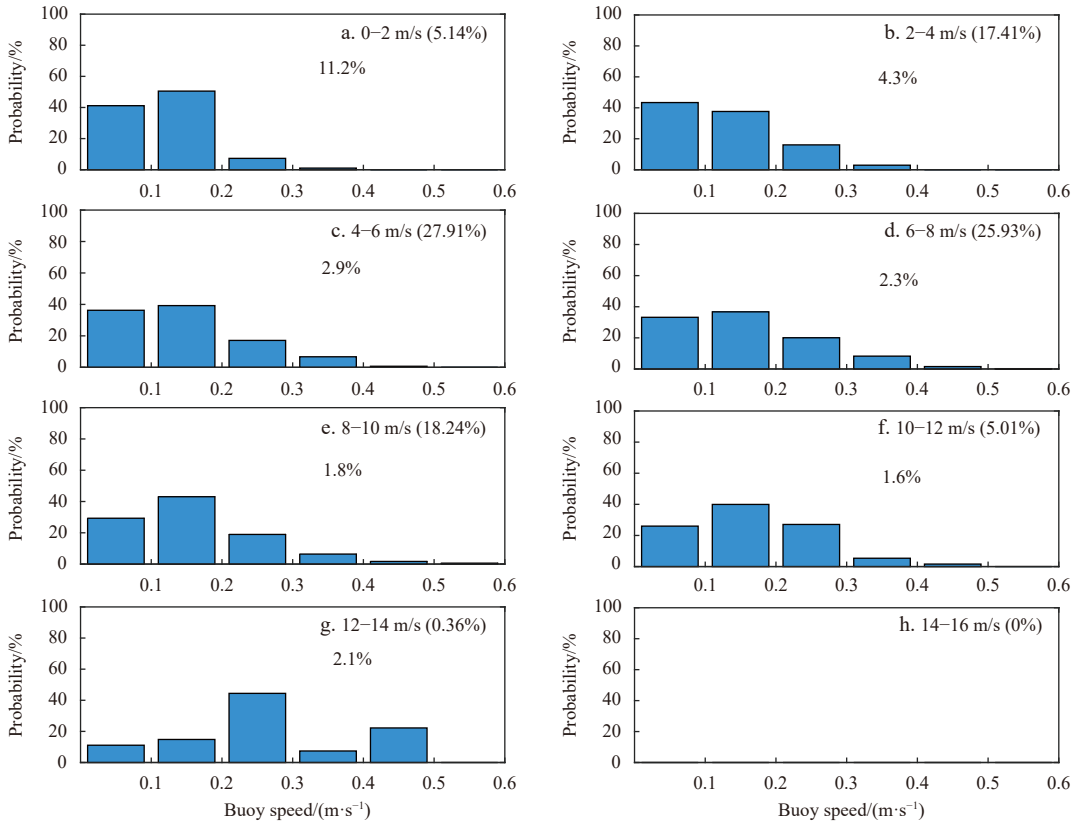

Fig. 11. Distribution of buoy velocity among Buoys A–D for 2 m/s magnitude bands of wind speed for ice concentrations <50%. The probability of each wind-speed class is shown in brackets, and the mean wind factor is shown below the wind-speed class.

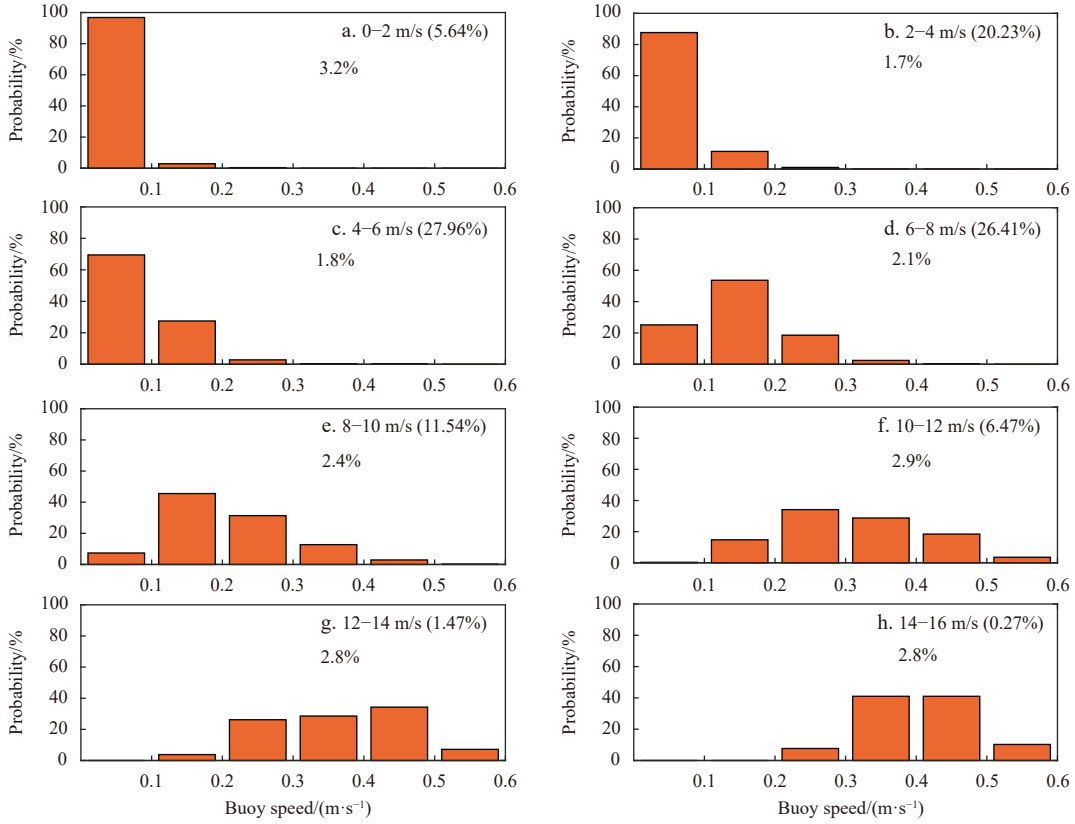

Fig. 12. Distribution of buoy velocity among Buoys A–D for 2 m/s magnitude bands of wind speed for ice concentrations >50%. The probability of each wind-speed class is shown in brackets, and the mean wind factor is shown below the wind-speed class.

gering 11.2%. At higher wind speeds, the WF dropped to approximately 2%. The distribution of wind speeds in each section is similar in Figs 11 and 12. In contrast, the buoy drift speed is mainly distributed in the interval of 0.1 m/s for wind speeds below 6 m/s, as shown in Fig. 12. At wind speeds above 6 m/s, the buoy drift speed was normally distributed. As the wind speeds increased, the WF first decreased and then increased and eventually remained at approximately 3%.

Similarly, the turning angle of buoys was closely related to the buoy working environment. Figures 13 and 14 show the buoy turning angle distribution at different wind speed magnitudes. With ice concentration below 50%, the buoy turning angle was distributed uniformly in all sections for wind speeds below 6 m/s, and the turning angle was mainly distributed in the intervals of 0°–90° at wind speeds above 12 m/s. In Fig. 14, the buoy turning angle was normally distributed when wind speeds were below 4 m/s. For wind speeds above 8 m/s, the buoy turning angle was mainly distributed between 0° and 45°. This result is consistent with that shown in Fig. 10.

5.3 *Inertial oscillation*

The increase in the inertial oscillation of buoy drift is caused by the sudden change in external forces, mainly owing to variations in the wind force and ice concentration. Based on the Fourier transformation, the energy variance in the normalized sea ice speed scalar exhibited a clear secondary maximum at semi-diurnal frequencies of approximately 2.0 cycles/d and this semi-diurnal signal was largely due to the inertial response (Gimbert et al., 2012a). The magnitudes of the semidiurnal frequency peak energies were closely related to sea ice concentration.

For all buoys, the amplitudes of the 12-h cycle remained high between August and mid-October 2018 (Fig. 15). Subsequently, the buoys entered the ice edge, and the inertially induced ice movement was damped with the advent of winter as the ice concentration and internal stress increased. Once buoys drifted into the MIZ, where the ice concentration rapidly decreased, the normalized amplitude at semi-diurnal frequencies increased slightly. However, in December, abnormal warm air currents occurred in the central Canadian Ocean Basin, which suddenly reduced the concentration of sea ice and significantly increased the amplitude of the buoy velocity. This phenomenon was also observed in February and March of 2019. This is consistent with the pan-Arctic analysis by Lei et al. (2016). They also found that the sea ice inertial response was the strongest during the melting season. Because of the kinetic energy dissipation caused by surface friction and internal ice stress, the ice strength is weakened, and the seasonal variation in sea ice movement mainly occurs in the seasonal ice area. On the contrary, it was almost negligible in the ice accumulation area. Therefore, the inertial component of ice motion is closely related to the seasonal and spatial variations in the ice state. With the continuous growth and consolidation of sea ice, the value of the motion amplitudes keeps decreasing to a minimum.

6 Discussion

Within the 9th CHINARE, eight TUT buoys were deployed in the open water of the Canadian Basin. Four TUT buoys remained in the packed ice as the ice grew and consolidated into a

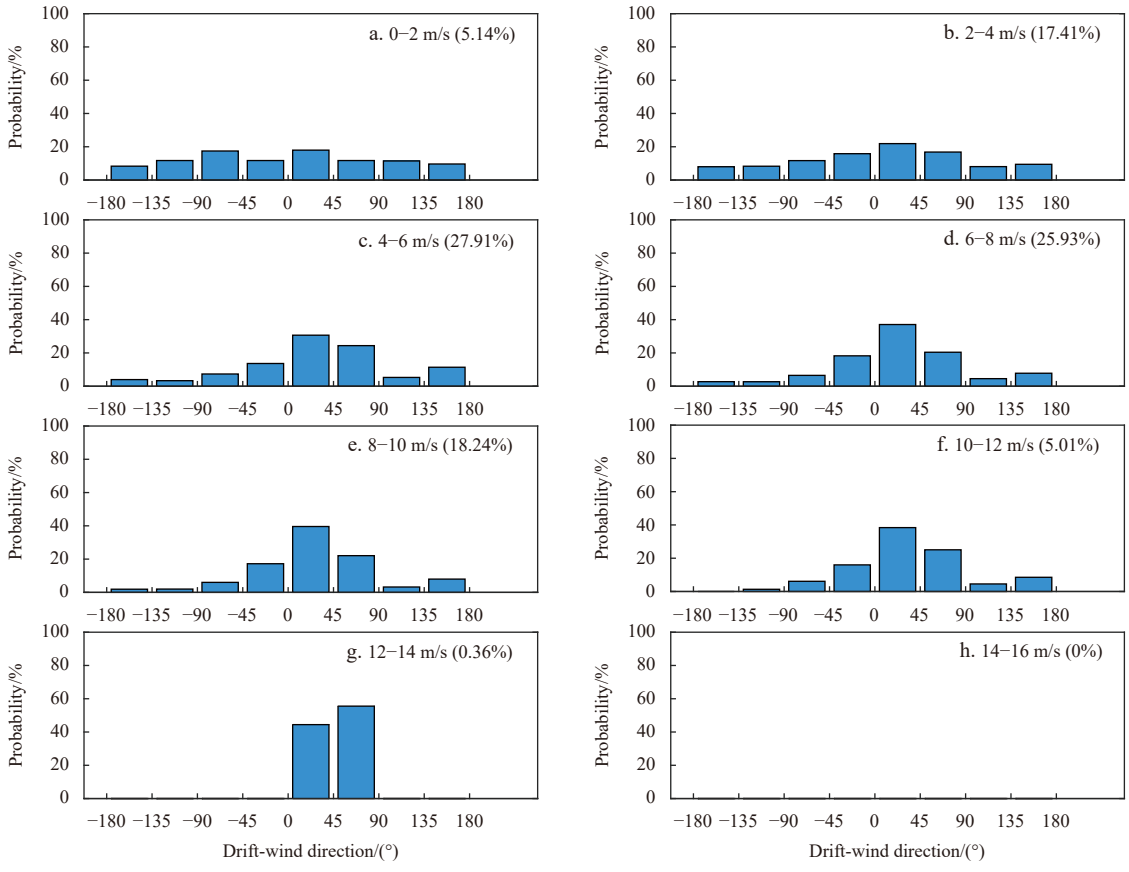

Fig. 13. Distribution of buoys drift turning angle with wind vectors for 2 m/s magnitude bands of wind speed for ice concentrations <50%. The probability of each wind-speed class is shown in brackets. Positive turning angle means buoys drift to the right of the wind.

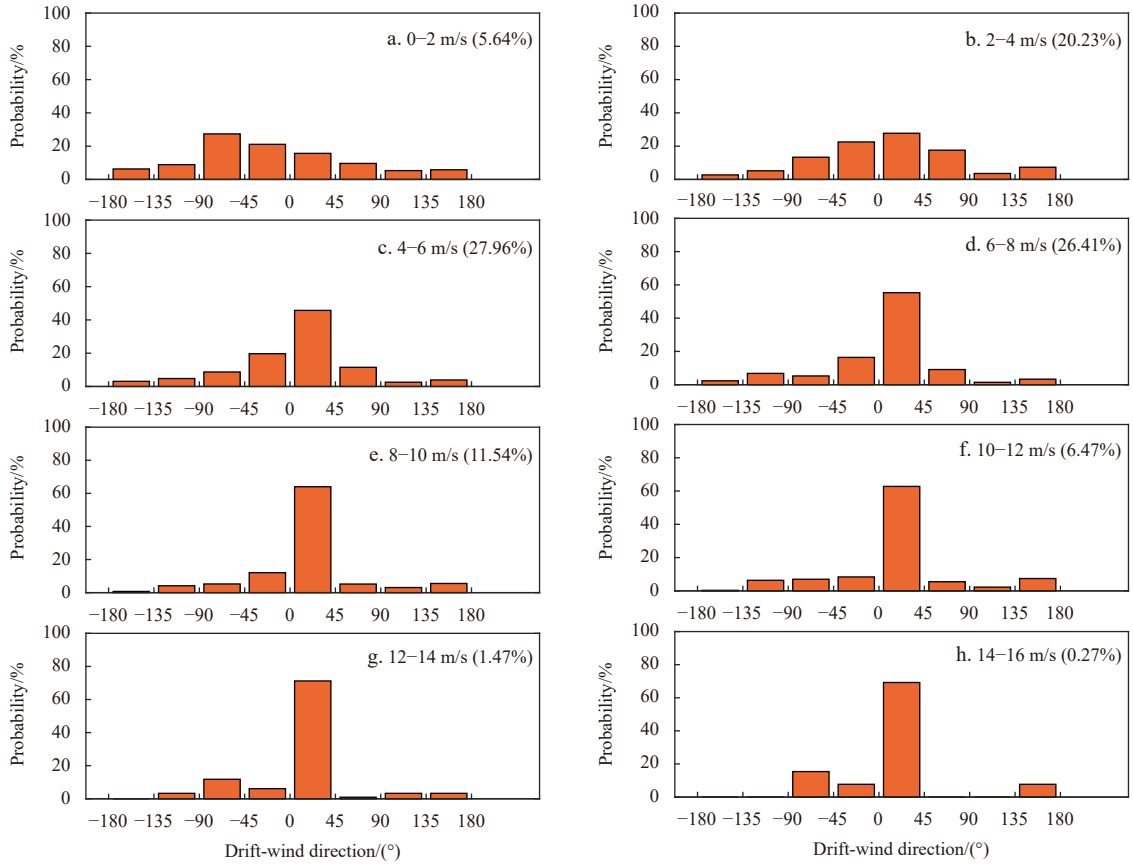

Fig. 14. Distribution of buoys drift turning angle with wind vectors for 2 m/s magnitude bands of wind speed for ice concentrations >50%. The probability of each wind-speed class is shown in brackets. Positive turning angle means buoys drift to the right of the wind.

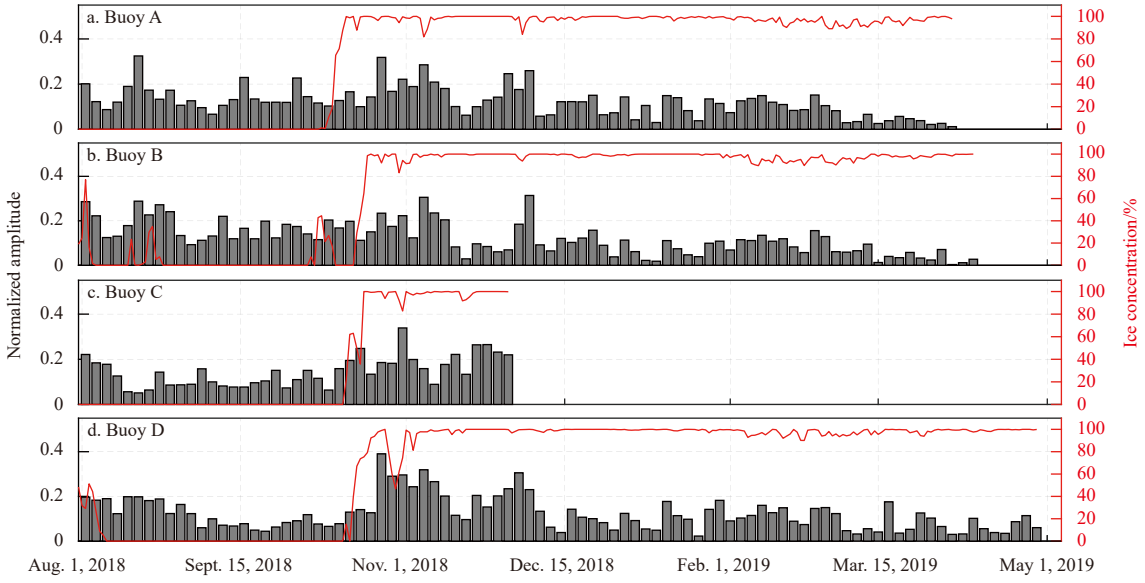

Fig. 15. Amplitude after Fourier transformation corresponding to the 12-h cycle of the normalized velocities for a sliding three-day window and near ice concentration of Buoys A–D.

coherent ice sheet successfully. The measurement covered the period from August 2018 to April 2019. In this study, we analysed the buoy drift characteristics during the procession from the open water to the ice zone based on a combination of observation and remote sensing data. The results showed that the drift has undergone distinct changes in the process which is closely related to sea ice growth and consolidation. With sea ice growing and gathering, the speed of buoys gradually decreased, and the drift-wind dir became more regular. This is required in a comprehensive sea ice model that is appropriate for the MIZ. Here, we discussed the changes in the movement of buoys and the implications of this study for future work.

During the operation of buoys in the Canadian Basin, our results showed that the high temporal resolution of the buoy position is an essential condition in the study of the MIZ. Compared to other studies, the measurement also shows that the velocity was highly intermittent before buoys entered the ice zone, and the trajectory is more winding than the packed ice (Doble, 2009). Therefore long intervals, such as satellite estimates (Gentemann et al., 2020; Yang et al., 2014), substantially underestimate the drift speed. If the position data were taken at only 1–3 d intervals, the drift estimates would be underestimated by 10%–30%. This indicates that the buoy drift can be over-simplified with a lower time resolution such as satellite-based data. To correctly describe ice kinematics and determine when the buoy entered the ice zone during the growth period, ground-truth data such as those provided by buoys are still needed (Shu et al., 2012).

Good agreement with the relationship among the indices and atmospheric circulation patterns is found based on remote sensing data (Wu, 2017). The wind vectors were usually clockwise in the study area and the anticyclonic wind intrudes from the south of the study area, as the BH and AO are low. Northerly wind is highly determined by the DA index and CAI (Wu et al., 2006). With the positive high DA index and CAI, the northerly wind almost across the whole study area. This phenomenon is likely to be more pronounced in the increasing ice-free Arctic (Lei et al., 2020). Moreover, our results show that the drift of the buoy has different responses to the wind in different months, mainly due to the changes in the ice conditions near the buoy. Good correlation coefficient between buoy drift and the wind only happened when the buoy was in the ice zone according to the ice concentration.

Remote sensing data was used to detect the ice conditions changes near the buoy. Sea ice concentration is the most direct indicator of whether the buoys enter the ice zone. It is closely linked to floe welding (Roach et al., 2018a). However, as it is affected by resolution, sea ice concentration cannot very accurately reflect the buoy information status. This explains why the sea ice concentration has a high value while all the buoys are deployed in open water. Studies on imagery provided by spaceborne Synthetic Aperture Radar (SAR) systems can be used to routinely derive ice thickness in the new ice region and detect the sea ice surface features (Aulicino et al., 2019; Wright and Polashenski, 2018). Open water, melt ponds submerged ice, snow and ice can be identified by the high resolution imagery, and the accuracy over 96% (Griebel, 2020).

Here, we combine the changes in the sea ice concentration, sea surface temperature, and buoy speed. The date when new ice around the buoy started to grow was assumed to have occurred in mid-October (Doble and Wadhams, 2006). Obtaining a more accurate time is essential for future study. Existing analysis on the SAR images has focused on the ice melting process, nevertheless. In this sense, we look forward to studying the ice growth process by using SAR imagery.

7 Conclusions

In this study, we analysed the characteristics of sea ice kinematics in the MIZ and compared the contrast in buoy dynamics from open water to the pack ice zone. The results showed a marked change in the correlation between the buoy drift and wind. The response of buoy drift to the wind is highly determined by the sea ice conditions near the buoy. The high amplitude and high frequency buoy motions ceasing rapidly as the buoy entered the ice zone. The correlation coefficient value remained below 0.3 as buoys in the open water in the first two or three months. After buoys drifted to the ice edge, the value increased remarkably to 0.7–0.9 in October for sea ice growth. Then, it began to decrease after February 2019, which has been caused by floe welding and ice cover consolidation (Heil et al., 2008).

Moreover, the distribution of drift-wind direction had an insignificant correlation with the wind while buoys were in open water. After November 2018, the angle between the wind heading and the buoy direction mainly within 45°, changed as the wind became weaker. Statistics were used to exclude the impact of seasonal. The results demonstrated that both drift speed and drift wind direction are notably associated with the ice state around the buoys. Only buoys entered the ice zone, the correlation coefficient between buoy drift and wind gets high. This can be used to determine whether the buoy entered the ice zone, which has a significant impact on the study of new ice growth. The inertial oscillation of the buoys also confirms this interpretation. The normalized amplitude was high for buoys in the open water. It decreased slightly when buoys drifted in the ice zone, where the ice concentration increased rapidly. This could greatly assist in determining whether buoys enter the ice zone, particularly for buoys with disposable observations in the International Arctic Buoy Program.

Acknowledgements

The authors gratefully acknowledge the supports of various foundations. The authors are grateful to the editor and anonymous reviewers whose comments have contributed to improving the quality.

References

Aksenov Y, Popova E E, Yool A, et al. 2017. On the future navigability of Arctic sea routes: High-resolution projections of the Arctic Ocean and sea ice. Marine Policy, 75: 300–317, doi: 10.1016/j.marpol.2015.12.027

Alam A, Curry J A. 1998. Evolution of new ice and turbulent fluxes over freezing winter leads. Journal of Geophysical Research: Oceans, 103(C8): 15783–15802, doi: 10.1029/98JC01188

Assmy P, Fernández-Méndez M, Duarte P, et al. 2017. Leads in Arctic pack ice enable early phytoplankton blooms below snow-covered sea ice. Scientific Reports, 7(1): 40850, doi: 10.1038/srep40850

Aulicino G, Wadhams P, Parmiggiani F. 2019. SAR pancake ice thickness retrieval in the terra nova bay (Antarctica) during the PIPERS expedition in winter 2017. Remote Sensing, 11(21): 2510, doi: 10.3390/rs11212510

Beitsch A, Kaleschke L, Kern S. 2014. Investigating high-resolution AMSR2 sea ice concentrations during the February 2013 fracture event in the Beaufort Sea. Remote Sensing, 6(5): 3841–3856, doi: 10.3390/rs6053841

Boutin G, Lique C, Ardhuin F, et al. 2020. Towards a coupled model to investigate wave–sea ice interactions in the Arctic marginal ice zone. The Cryosphere, 14(2): 709–735, doi: 10.5194/tc-14-709-2020

Clem K R, Fogt R L, Turner J, et al. 2020. Record warming at the South Pole during the past three decades. Nature Climate Change, 10(8): 762–770, doi: 10.1038/s41558-020-0815-z

Delhasse A, Kittel C, Amory C, et al. 2020. Brief communication: Evaluation of the near-surface climate in ERA5 over the Greenland Ice Sheet. The Cryosphere, 14(3): 957–965, doi: 10.5194/tc-14-957-2020

Doble M J. 2009. Simulating pancake and frazil ice growth in the Weddell Sea: A process model from freezing to consolidation. Journal of Geophysical Research: Oceans, 114(C9): C09003

Doble M J, Wadhams P. 2006. Dynamical contrasts between pancake and pack ice, investigated with a drifting buoy array. Journal of Geophysical Research: Oceans, 111(C11): C11S24

Gentemann C L, Scott J P, Mazzini P L F, et al. 2020. Saildrone: Adapt-

ively sampling the marine environment. Bulletin of the American Meteorological Society, 101(6): E744–E762, doi: 10.1175/BAMS-D-19-0015.1
Gimbert F, Jourdain N C, Marsan D, et al. 2012a. Recent mechanical weakening of the Arctic sea ice cover as revealed from larger inertial oscillations. Journal of Geophysical Research: Oceans, 117(C11): C00J12
Gimbert F, Marsan D, Weiss J, et al. 2012b. Sea ice inertial oscillations in the Arctic Basin. The Cryosphere, 6(5): 1187–1201, doi: 10.5194/tc-6-1187-2012
Griebel J. 2020. Improvements and analyzes of sea ice drift and deformation retrievals from SAR images [dissertation]. Bremen: University of Bremen
Haller M, Brümmer B, Müller G. 2014. Atmosphere–ice forcing in the transpolar drift stream: results from the DAMOCLES ice-buoy campaigns 2007–2009. The Cryosphere, 8(1): 275–288, doi: 10.5194/tc-8-275-2014
Heil P, Hutchings J K, Worby A P, et al. 2008. Tidal forcing on sea-ice drift and deformation in the western Weddell Sea in early austral summer, 2004. Deep-Sea Research Part II: Topical Studies in Oceanography, 55(8–9): 943–962, doi: 10.1016/j.dsr2.2007.12.026
Horvat C, Tziperman E. 2017. The evolution of scaling laws in the sea ice floe size distribution. Journal of Geophysical Research: Oceans, 122(9): 7630–7650, doi: 10.1002/2016JC012573
Howell S E L, Tivy A, Yackel J J, et al. 2008. Changing sea ice melt parameters in the Canadian Arctic Archipelago: Implications for the future presence of multiyear ice. Journal of Geophysical Research: Oceans, 113(C9): C09030
Hutchings J K, Hibler W D III. 2008. Small-scale sea ice deformation in the Beaufort Sea seasonal ice zone. Journal of Geophysical Research: Oceans, 113(C8): C08032
Itkin P, Spreen G, Hvidegaard S M, et al. 2018. Contribution of deformation to sea ice mass balance: A case study from an N-ICE2015 storm. Geophysical Research Letters, 45(2): 789–796, doi: 10.1002/2017GL076056
Lee C M, Thomson J, The Marginal Ice Zone Team, et al. 2017. An autonomous approach to observing the seasonal ice zone in the western Arctic. Oceanography, 30(2): 56–68, doi: 10.5670/oceanog.2017.222
Lei Ruibo, Gui Dawei, Yuan Zhouli, et al. 2020. Characterization of the unprecedented polynya events north of Greenland in 2017/2018 using remote sensing and reanalysis data. Acta Oceanologica Sinica, 39(9): 5–17, doi: 10.1007/s13131-020-1643-8
Lei Ruibo, Heil P, Wang Jia, et al. 2016. Characterization of sea-ice kinematic in the Arctic outflow region using buoy data. Polar Research, 35(1): 22658, doi: 10.3402/polar.v35.22658
Lei Ruibo, Hoppmann M, Cheng Bin, et al. 2021. Seasonal changes in sea ice kinematics and deformation in the Pacific sector of the Arctic Ocean in 2018/19. The Cryosphere, 15(3): 1321–1341, doi: 10.5194/tc-15-1321-2021
Leppäranta M. 2011. The Drift of Sea Ice. 2nd ed. Berlin: Springer, 51–56
Liu Yue, Pang Xiaoping, Zhao Xi, et al. 2021. Prediction of the Antarctic marginal ICE zone extent based upon its multifractal property. Fractals, 29(2): 2150035, doi: 10.1142/S0218348X21500353
Lund B, Graber H C, Persson P O G, et al. 2018. Arctic sea ice drift measured by shipboard marine radar. Journal of Geophysical Research: Oceans, 123(6): 4298–4321, doi: 10.1029/2018JC013769
Lüpkes C, Vihma T, Birnbaum G, et al. 2008. Influence of leads in sea ice on the temperature of the atmospheric boundary layer during polar night. Geophysical Research Letters, 35(3): L03805
Manda A, Takahashi T, Komori S, et al. 2002. Validation of a new type of Lagrangian drifter using a GPS cellular phone. International Journal of Offshore and Polar Engineering, 12(3): 213–216
Moore G W K, Schweiger A, Zhang J, et al. 2018. Collapse of the 2017 winter Beaufort High: A response to thinning sea ice?. Geophysical Research Letters, 45(6): 2860–2869, doi: 10.1002/2017GL076446
Nansen F. 1902. Oceanography of the North Polar basin: the Norwegian North Polar Expedition 1893–96. Scientific Results, 3(9): 427
Notz D, Community S. 2020. Arctic sea ice in CMIP6. Geophysical Research Letters, 47(10): e2019GL086749
Qu Meng, Pang Xiaoping, Zhao Xi, et al. 2021. Spring leads in the Beaufort Sea and its interannual trend using Terra/MODIS thermal imagery. Remote Sensing of Environment, 256: 112342, doi: 10.1016/j.rse.2021.112342
Rampal P, Weiss J, Marsan D. 2009. Positive trend in the mean speed and deformation rate of Arctic sea ice, 1979–2007. Journal of Geophysical Research: Oceans, 114(C5)
Roach L A, Horvat C, Dean S M, et al. 2018a. An emergent sea ice floe size distribution in a global coupled ocean-sea ice model. Journal of Geophysical Research: Oceans, 123(6): 4322–4337, doi: 10.1029/2017JC013692
Roach L A, Smith M M, Dean S M. 2018b. Quantifying growth of pancake sea ice floes using images from drifting buoys. Journal of Geophysical Research: Oceans, 123(4): 2851–2866, doi: 10.1002/2017JC013693
Screen J A, Bracegirdle T J, Simmonds I. 2018. Polar climate change as manifest in atmospheric circulation. Current Climate Change Reports, 4(4): 383–395, doi: 10.1007/s40641-018-0111-4
Serreze M C, Barrett A P. 2011. Characteristics of the Beaufort Sea high. Journal of Climate, 24(1): 159–182, doi: 10.1175/2010JCLI3636.1
Shen H H, Ackley S F. 1991. A one-dimensional model for wave-induced ice-floe collisions. Annals of Glaciology, 15: 87–95, doi: 10.3189/1991AoG15-1-87-95
Shu Qi, Ma Hongyu, Qiao Fangli. 2012. Observation and simulation of a floe drift near the North Pole. Ocean Dynamics, 62(8): 1195–1200, doi: 10.1007/s10236-012-0554-4
Spreen G, Kaleschke L, Heygster G. 2008. Sea ice remote sensing using AMSR-E 89-GHz channels. Journal of Geophysical Research: Oceans, 113(C2): C02S03
Stroeve J C, Kattsov V, Barrett A, et al. 2012. Trends in Arctic sea ice extent from CMIP5, CMIP3 and observations. Geophysical Research Letters, 39(16)
Strong C, Foster D, Cherkaev E, et al. 2017. On the definition of marginal ice zone width. Journal of Atmospheric and Oceanic Technology, 34(7): 1565–1584, doi: 10.1175/JTECH-D-16-0171.1
Strong C, Rigor I G. 2013. Arctic marginal ice zone trending wider in summer and narrower in winter. Geophysical Research Letters, 40(18): 4864–4868, doi: 10.1002/grl.50928
Taylor M H, Losch M, Bracher A. 2013. On the drivers of phytoplankton blooms in the Antarctic marginal ice zone: A modeling approach. Journal of Geophysical Research: Oceans, 118(1): 63–75, doi: 10.1029/2012JC008418
Timmermans M L, Marshall J. 2020. Understanding Arctic Ocean circulation: a review of ocean dynamics in a changing climate. Journal of Geophysical Research: Oceans, 125(4): e2018JC014378
Uotila J, Vihma T, Launiainen J. 2000. Response of the Weddell Sea pack ice to wind forcing. Journal of Geophysical Research: Oceans, 105(C1): 1135–1151, doi: 10.1029/1999JC900265
Vichi M, Eayrs C, Alberello A, et al. 2019. Effects of an explosive polar cyclone crossing the Antarctic marginal ice zone. Geophysical Research Letters, 46(11): 5948–5958, doi: 10.1029/2019GL082457
Vihma T, Tisler P, Uotila P. 2012. Atmospheric forcing on the drift of Arctic sea ice in 1989–2009. Geophysical Research Letters, 39(2): L02501
Vinje T. 2001. Anomalies and trends of sea-ice extent and atmospheric circulation in the Nordic Seas during the period 1864–1998. Journal of Climate, 14(3): 255–267, doi: 10.1175/1520-0442(2001)014<0255:AATOSI>2.0.CO;2
Wang Jia, Zhang Jinlun, Watanabe E, et al. 2009. Is the Dipole Anomaly a major driver to record lows in Arctic summer sea ice extent?. Geophysical Research Letters, 36(5): L05706
Weeks W F, Ackley S F. 1986. The growth, structure, and properties of

sea ice. In: Untersteiner N, ed. The Geophysics of Sea Ice. NATO ASI Series (Series B: Physics). Boston: Springer, 9–164

Willmes S, Heinemann G. 2016. Sea-ice wintertime lead frequencies and regional characteristics in the Arctic, 2003–2015. Remote Sensing, 8(1): 4

Wright N C, Polashenski C M. 2018. Open-source algorithm for detecting sea ice surface features in high-resolution optical imagery. The Cryosphere, 12(4): 1307–1329, doi: 10.5194/tc-12-1307-2018

Wu Bingyi. 2017. Winter atmospheric circulation anomaly associated with recent Arctic winter warm anomalies. Journal of Climate, 30(21): 8469–8479, doi: 10.1175/JCLI-D-17-0175.1

Wu Bingyi, Wang Jia, Walsh J E. 2006. Dipole anomaly in the winter Arctic atmosphere and its association with sea ice motion. Journal of Climate, 19(2): 210–225, doi: 10.1175/JCLI3619.1

Yang H, Choi J K, Park Y J, et al. 2014. Application of the Geostationary Ocean Color Imager (GOCI) to estimates of ocean surface currents. Journal of Geophysical Research: Oceans, 119(6): 3988–4000, doi: 10.1002/2014JC009981

Yu Yining, Xiao Wanxin, Zhang Zhilun, et al. 2021. Evaluation of 2-m air temperature and surface temperature from ERA5 and ERA-I using buoy observations in the Arctic during 2010–2020. Remote Sensing, 13(14): 2813, doi: 10.3390/rs13142813

Zhang Jinlun, Lindsay R, Schweiger A, et al. 2012. Recent changes in the dynamic properties of declining Arctic sea ice: A model study. Geophysical Research Letters, 39(20): L20503

Zhang Jinlun, Schweiger A, Steele M, et al. 2015. Sea ice floe size distribution in the marginal ice zone: Theory and numerical experiments. Journal of Geophysical Research: Oceans, 120(5): 3484–3498, doi: 10.1002/2015JC010770

Zuo Guangyu, Dou Yinke, Chang Xiaomin, et al. 2018a. Design and performance analysis of a multilayer sea ice temperature sensor used in polar region. Sensors, 18(12): 4467

Zuo Guangyu, Dou Yinke, Lei Ruibo. 2018b. Discrimination algorithm and procedure of snow depth and sea ice thickness determination using measurements of the vertical ice temperature profile by the ice-tethered buoys. Sensors, 18(12): 4162, doi: 10.3390/s18124162